Since January 2020 Elsevier has created a COVID-19 resource centre with free information in English and Mandarin on the novel coronavirus COVID-19. The COVID-19 resource centre is hosted on Elsevier Connect, the company's public news and information website.

The American Journal of Pathology, Vol. 193, No. 7, July 2023

ELSEVIER

The American Journal of
PATHOLOGY

ajp.amjpathol.org

IMMUNOPATHOLOGY AND INFECTIOUS DISEASES

Murine Coronavirus Disease 2019 Lethality Is Characterized by Lymphoid Depletion Associated with Suppressed Antigen-Presenting Cell Functionality

Yu Jin Lee,* Sang Hyeok Seok,* Na Yun Lee,* Hee Jin Choi,* Yoon Woo Lee,† Hee Jung Chang,† Ji-Yeon Hwang,‡ Da In On,§ Hyun Ah Noh,§ Su-Bin Lee,¶ Ho-Keun Kwon,¶ Jun-Won Yun,‖ Jeon-Soo Shin,¶** Jun-Young Seo,** Ki Taek Nam,** Ho Lee,†† Ho Young Lee,† Jun Won Park,* and Je Kyung Seong§‡‡

From the Division of Biomedical Convergence, College of Biomedical Science, Kangwon National University, ChunCheon; the Department of Nuclear Medicine† and the Preclinical Research Center,‡ Seoul National University Bundang Hospital, Seoul; the Korea Mouse Phenotyping Center,§ the College of Veterinary Medicine,‖ and the Laboratory of Developmental Biology and Genomics,‡‡ Research Institute for Veterinary Science, and BK 21 PLUS Program for Creative Veterinary Science Research, College of Veterinary Medicine, Seoul National University, Seoul; the Department of Microbiology and Immunology,¶ the Severance Biomedical Science Institute,** and the Brain Korea 21 PLUS Project for Medical Science, Yonsei University College of Medicine, Seoul; and the Graduate School of Cancer Science and Policy,†† National Cancer Center, Goyang, Republic of Korea*

Accepted for publication March 16, 2023.

Address correspondence to Je Kyung Seong, Ph.D., D.V.M., Korea Mouse Phenotyping Center, Seoul National University, Seoul 08826, Republic of Korea; or Jun Won Park, Ph.D., D.V.M., Division of Biomedical Convergence, College of Biomedical Science, Kangwon National University, Chun-Cheon, Republic of Korea. E-mail: snumouse@snu.ac.kr or jwpark@kangwon.ac.kr.

The disease severity of coronavirus disease 2019 (COVID-19) varies considerably from asymptomatic to serious, with fatal complications associated with dysregulation of innate and adaptive immunity. Lymphoid depletion in lymphoid tissues and lymphocytopenia have both been associated with poor disease outcomes in patients with COVID-19, but the mechanisms involved remain elusive. In this study, human angiotensin-converting enzyme 2 (h*ACE2*) transgenic mouse models susceptible to severe acute respiratory syndrome coronavirus 2 (SARS-CoV-2) infection were used to investigate the characteristics and determinants of lethality associated with the lymphoid depletion observed in SARS-CoV-2 infection. The lethality of Wuhan SARS-CoV-2 infection in K18-h*ACE2* mice was characterized by severe lymphoid depletion and apoptosis in lymphoid tissues related to fatal neuroinvasion. The lymphoid depletion was associated with a decreased number of antigen-presenting cells (APCs) and their suppressed functionality below basal levels. Lymphoid depletion with reduced APC function was a specific feature observed in SARS-CoV-2 infection but not in influenza A infection and had the greatest prognostic value for disease severity in murine COVID-19. Comparison of transgenic mouse models resistant and susceptible to SARS-CoV-2 infection revealed that suppressed APC function could be determined by the h*ACE2* expression pattern and interferon-related signaling. Thus, we demonstrated that lymphoid depletion associated with suppressed APC function characterizes the lethality of COVID-19 mouse models. Our data also suggest a potential therapeutic approach to prevent the severe progression of COVID-19 by enhancing APC functionality. *(Am J Pathol 2023, 193: 866–882; https://doi.org/10.1016/j.ajpath.2023.03.008)*

Coronavirus disease 2019 (COVID-19) has rapidly spread worldwide, posing a serious threat to global health. The disease severity of COVID-19 varies considerably from asymptomatic to serious, with fatal complications. In fatal COVID-19 cases, severe acute respiratory syndrome coronavirus 2 (SARS-CoV-2) spreads and persists throughout the human body, including the brain.[1] The components of innate and adaptive immunity are dysregulated in symptomatic adult patients.[1,2] The risk of developing severe disease has been associated with dysregulated immune responses in patients.[2] In particular, lymphopenia and lymphoid depletion in lymphoid tissues have been associated with poor disease outcomes in

Supported by grants of the National Research Foundation funded by the Korean government: 2013M3A9D5072550 (J.K.S.), 2021M3H9A1030260 (J.K.S.), 2013M3A9D5072560 (H.Y.L.), RS-2023-00208984 (J.W.P.), and 2019R1A6A1A03032869 (H.-K.K.).

Y.J.L., S.H.S., and N.Y.L. contributed equally to this work.

Disclosures: None declared.

https://doi.org/10.1016/j.ajpath.2023.03.008

patients with COVID-19.[3–6] However, the mechanisms involved remain elusive, partially due to limitations in evaluating immunologic factors of clinical samples, which could be affected by numerous factors, such as underlying diseases, age, sex, exposed environments, and eating habits.[7] Therefore, investigating the underlying factors of the risk of developing severe disease in terms of immunodynamics under well-controlled infectious conditions based on animal models is essential to understanding the mortality and immunologic factors that contribute to disease severity.

The human angiotensin-converting enzyme 2 (h*ACE2*) protein is the functional receptor for SARS-CoV-2 to enter cells.[8] Although conventional laboratory mice cannot be infected with SARS-CoV-2, h*ACE2* expression as a transgene by various promoters supports SARS-CoV-2 binding.[8–11] h*ACE2* transgenic mice exhibit susceptibility to SARS-CoV-2 infection but vary in disease severity, depending on the promoter used to drive h*ACE2* expression.[11] Transgenic mice expressing h*ACE2* under the cytokeratin 18 promoter (K18-h*ACE2*) represent a lethal model of SARS-CoV-2 infection.[8–11] They develop lung inflammation accompanied by high viral replication, experience significant weight loss, and experience decreased body temperature over the course of infection. This mouse model has been most widely utilized in the evaluation of vaccines and therapeutic efficacies for COVID-19 treatment. In a previous study, transgenic mice expressing h*ACE2* under the Cytomegalovirus (CMV) early enhancer/chicken β actin (CAG) promoter (CAG-h*ACE2*-FVB) were established.[11] K18-h*ACE2* mice exhibited definitive lethality, but CAG-h*ACE2* mice survived, suggesting that K18-h*ACE2* mice are relatively susceptible to SARS-CoV-2 and that CAG-h*ACE2* mice are resistant to SARS-CoV-2. An in-depth comparative study of lethality in mouse models showing various disease severity could provide clues to elucidate the determinants and immunologic consequences for developing mortality to SARS-CoV-2.

On the basis of preliminary data, viral doses in plaque-forming units (PFUs) were established for nasal inoculation to make K18-*hACE2* mice exhibit a diverse range of disease severity. This lethal murine COVID-19 model exhibited viral invasion into the brain.[12,13] Herein, this setup was used to investigate the mechanism of mortality and the immunologic factors that contribute to disease severity by examining correlations between clinicohistopathologic features, immune profiles of immune organs, and disease severity. The lethality of SARS-CoV-2–infected mice was characterized by severe atrophy and apoptosis of lymphoid tissues associated with brain infection. To investigate the possible mechanisms and determinants of this lethality observed in SARS-CoV-2 infection, comparative studies were performed according to mouse models, viral inoculation routes, and SARS-CoV-2 strains. This work provides useful information to better understand the immune dysregulation associated with COVID-19 severity and a potential therapeutic approach to prevent the severe progression of COVID-19.

Materials and Methods

Animal Models, Cell Line, and Viral Culture

The mice (8 weeks old; male) used in these studies were obtained from the Jackson Laboratory [Bar Harbor, ME; B6.Cg-Tg (K18-*ACE2*)2Prlman/J] and are congenic on the C57BL/6 background. Two different lineages of human *ACE2* gene transgenic FVB mice using Keratin 18 (Krt18) or CAG promoters were produced in the previous study.[11] All protocols were approved by the Institutional Animal Care and Use Committee of the Seoul National University Bundang Hospital (Seoul, Republic of Korea; Institutional Animal Care and Use Committee number BA-2008-301-071-05). The Ji Seok Young Research Centre is fully accredited by the Association for Assessment and Accreditation of Laboratory Animal Care. All animals were cared for in accordance with the Institute for Laboratory Animal Research *Guide for the Care and Use of Laboratory Animals*.[14] The Seoul National University Bundang Hospital Institutional Biosafety Committee approved the procedures for sample handling, inactivation, and transfer from animal biosafety level 3 containment.

The original Wuhan strain of SARS-CoV-2 (accession number: NCCP43326/Korea), SARS-CoV-2 Delta variant (accession number: NCCP43390/Korea), SARS-CoV-2 Omicron variant (BA.1; accession number: NCCP43408/Korea), and influenza A virus (H1/N1; accession number: NCCP42467/Korea) were procured from the Korea Centers for Disease Control and Prevention (*https://nccp.kdca.go.kr*, last accessed April 20, 2023). Vero E6 cell (CRL-1586) was procured from the Korea Microbial Resource Centre. Vero E6 was maintained in Dulbecco's modified Eagle's medium (Life Technologies, Carlsbad, CA) containing 10% fetal bovine serum (Life Technologies). SARS-CoV-2 was inoculated with Vero E6 cells to confirm the cytopathic effect on the third day; virus titer was measured by plaque assay and stored at −70°C.

All mice were infected intranasally with viruses in a total volume of 50 μL Dulbecco's modified Eagle's medium. The mice were lightly anesthetized with ketamine (20 mg/kg)/xylazine (10 mg/kg). The weight, temperature, and health of the mice were monitored daily. The mice were sacrificed with CO_2 chamber on day 0 and the first, second, and fifth days post infection (dpi). All experiments with SARS-CoV-2 were performed in a biosafety level 3 laboratory at the Seoul National University Bundang Hospital.

Virus Titration

The 50% tissue culture infectious dose (TCID50) was calculated according to the Reed-Muench method. The Vero E6 cells were seeded in 12-well plates at a concentration of

3×10^5 cells per well and incubated to form a monolayer 1 day before the plaque assay. The cells were infected for 1 hour in duplicate with 10-fold serial dilutions of SARS-CoV-2 and overlaid with a 0.3% SeaPlaque (LONZA, Basel, Switzerland) agarose medium containing 2% fetal bovine serum. After 72 hours of incubation, the cells infected with viruses were fixed by 4% (v/v) paraformaldehyde (Biosesang, Seongnam, Republic of Korea) for 1 hour and then stained using a crystal violet solution (548-62-9; Sigma-Aldrich, St. Louis, MO). The infectious virus titers were measured in PFUs per milliliter.

Histopathology

Lung, spleen, submandibular lymph node, and brain tissues were fixed in neutral-buffered 10% formalin for 1 day and processed using a standard method. The paraffin-embedded sections (3 μm thick) were stained with hematoxylin and eosin. The lesions were graded using a semiquantitative scale based on the percentage of tissue affected by pathologic changes as follows: 0, absent; 1, minimal, <10% of tissue affected; 2, mild, >10% but <25% of tissue affected; 3, moderate, >25% but <50% of tissue affected; 4, moderately severe, >50% but <75% of tissue affected; or 5, severe, >75% of tissue affected. The pulmonary lesions were evaluated on the basis of the presence and abundance of the following: pulmonary inflammation, involving the perivascular/peribronchial spaces with a moderate number of inflammatory cells surrounding the regions and interstitial spaces with more than five inflammatory cells in each alveolar space; and pulmonary edema, involving the perivascular spaces exhibiting edematous cuffs and alveolar edematous spaces. For the evaluation of the splenic lesions, the scoring for apoptosis in the white pulp was determined on the basis of the extent of the area affected. Scoring of white pulp atrophy was based on the extent of the size reduction compared with normal splenic white pulp. The degree of villous atrophy in the duodenum was scored on the basis of the changed shape (convolutions) and the decreased length of the villi. Histopathologic scores were determined by more than two veterinary pathologists (J.W.P. and K.T.N.).

Immunohistochemistry and Digital Analysis

The replicate paraffin sections were dewaxed, rehydrated, and subjected to antigen retrieval by heating at 100°C for 20 minutes in 0.01 mol/L citrate buffer (pH 6.0; C9999; Sigma-Aldrich). The ImmPRESS Peroxidase Polymer kit (Vector Laboratories, Burlingame, CA) was used for immunostaining in accordance with the manufacturer's protocol. Briefly, the slides were incubated with 2.5% horse serum for blocking and then incubated for 30 minutes at room temperature with the primary antibodies. Rabbit anti−SARS-CoV-2 nucleocapsid (Genetex, Irvine, CA), rabbit anti−influenza A nucleoprotein (Genetex), rabbit anti-CD11c (Cell Signaling Technology, Danvers, MA), rabbit anti-CD8 (Cell Signaling Technology), rabbit anti-CD4 (Cell Signaling Technology), rabbit anti-CD19 (Cell Signaling Technology), rat anti-CD3 (Abcam, Cambridge, UK), rabbit anti-F4/80 (Cell Signaling Technology), rabbit anti−forkhead box P3 (Foxp3; Cell Signaling Technology), rabbit anti-CD11b (Novus Biologicals, Centennial, CO), rat anti−major histocompatibility complex class II (MHCII; eBioscience, San Diego, CA), and rabbit anti-*ACE2* (Abcam) were used as primary antibodies. After washing, the slides were incubated for 30 minutes with the appropriate peroxidase polymer-linked secondary antibodies. The slides were subjected to colorimetric detection with the ImmPact diaminobenzidine substrate (SK-4105; Vector Laboratories). The slides were counterstained with Meyer's hematoxylin for 10 seconds. Negative controls were performed by omitting the primary antibody and substituting it with diluent.

For digital pathology, immunohistochemistry (IHC) slides were digitally scanned using Pannoramic SCAN slide scanner (3D HISTECH, Budapest, Hungary) at ×40 magnification. Aperio Nuclear V9 algorithm version 11.0.0.725 (Aperio Technologies, Vista, CA) was used to detect the CD4, CD8, CD11c, CD3, CD19, F4/80, Foxp3, and CD11b diaminobenzidine signals and count positive stained cells. First, the parameters were adjusted in this algorithm to accurately match the manual count of stained cells by a pathologist (J.W.P.) with automated counts obtained from the tuned algorithms. The set of tuned parameters for each marker was saved and used to run analysis on each tissue. The density of immune cell marker−positive cells was calculated by dividing the number of positive cells by the area examined. Representative analyzed images of IHC staining with high and low positive numbers for CD11c are shown in Supplemental Figure S1.

Immunofluorescence Staining

Formalin-fixed, paraffin-embedded slides were deparaffinized and sequentially rehydrated using ethanol. The slides were immersed in antigen retrieval solution (Dako, Santa Clara, CA) and incubated for antigen retrieval at high pressure using a cooker. After cooking, the slides were incubated with 2.5% horse serum in phosphate-buffered saline (PBS) for blocking and then incubated overnight at 4°C with the primary antibodies. Mouse anti−SARS-CoV-2 nucleocapsid (Sino Biological, Beijing, China), rabbit anti-CD11c (Cell Signaling Technology), rabbit anti-CD19 (Cell Signaling Technology), rat anti-CD3 (Abcam), rat anti-MHCII (eBioscience), rabbit anti-podoplanin (PDPN; Santa Cruz Biotechnology, Dallas, TX), goat anti−surfactant protein C (SP-C; Santa Cruz Biotechnology), rabbit anti-CD31 (Abcam), and rabbit anti−transmembrane protein 173 (TMEM173; Proteintech, Rosemont, IL) were used as primary antibodies. Each primary antibody derived from diverse species was detected with the use of Alexa488-conjugated,

Alexa568-conjugated, and Alexa647-conjugated secondary antibodies (secondary antibodies all from Invitrogen, Waltham, MA). Nuclear staining was performed with the use of DAPI (Abbkine, Wuhan, China). Confocal images were taken with a confocal microscope (Ts2; Nikon, Tokyo, Japan) of Kangwon Center for System Imaging.

In Situ Hybridization

Mouse *Sftpc* mRNA and SARS-CoV-2 spike protein mRNA were detected by *in situ* hybridization using RNAscope Probes (ACD, Bio-Techne, Minneapolis, MN) and RNAscope 2.5 HD Duplex Assay (322,436; ACD, Bio-Techne). Briefly, paraffin sections were retrieved in a boiling buffer and treated by protease for 30 minutes, and *in situ* hybridization was performed according to the manufacturer's protocol.

Cell Isolation and Flow Cytometry

To isolate cells from inflamed tissues, lung tissues were cut into four pieces and gently stirred in flasks with solution [PBS containing 25 mL 10 mmol/L EDTA, 3% fetal bovine serum (HyClone Laboratories, Logan, UT), 20 mmol/L HEPES, and 1 mmol/L sodium pyruvate) for 30 minutes at 37°C. The segments were washed three times with PBS and digested with 5 mL RPMI 1640 medium containing 1 mg/mL of type V collagenase (Sigma-Aldrich) for 45 minutes at 37°C. Finally, the soup containing ear total cell was centrifuged and cultured in T-cell media. For the surface marker staining, cells were washed with ice-cold PBS, resuspended in 100 μL of PBS, and stained with anti−CD45-APC-R700 (BD Biosciences, Franklin Lakes, NJ), anti−T-cell receptor beta (TCRb)-APC/Fire750 (BD Biosciences), anti−MHCII-peridinin chlorophyll protein complex (PerCP)-Cy5.5 (BD Biosciences), and anti−CD19-phycoerythrin (PE)/Cy7 (Biolegend, San Diego, CA). Dead cells were excluded using LiveDead Fixable Viability dye (Invitrogen). Samples were acquired using ID7000 (Sony, Tokyo, Japan), and data were analyzed using FlowJo software version 10 (Tree Star, Ashland, OR).

Statistical Analysis

Statistical analyses were performed with the GraphPad Prism software version 8 (San Diego, CA). Error bars indicate the SDs of the mean. Significance is indicated as follows: $*P \leq 0.05$, $**P \leq 0.01$, and $***P \leq 0.001$.

Results

K18-h*ACE2* Mice Represent a Lethal Animal Model for Severe COVID-19 Exhibiting Lymphoid Depletion

In the eight non-clinical tests performed in the same facility, 86 K18-h*ACE2* mice were intranasally infected with 1×10^5 PFUs of the original Wuhan strain of SARS-CoV-2 and were followed up until 7 dpi (Figure 1A). Over the course of infection at 7 dpi, the infected mice experienced rapid weight loss (Figure 1B) and decreased body temperature (Figure 1C). All infected mice survived, but most of them were moribund. On the basis of body weight and temperature, the infected mice showed a diverse range of disease severity at 7 dpi. The mean weight loss at 7 dpi was −21.4% (range, 2.6% to −30.4%; SD = 7.809) (Figure 1B). The mean body temperature at 7 dpi was 25.0°C (range, 18.2°C to 36.9°C; SD = 5.688) (Figure 1C). With lethality defined as >25% weight loss and/or <30°C body temperature, the mortality rate of infected mice reached approximately 80%.

Organ weight was measured during necropsy (Figure 1D). Lung weight was increased and spleen weight was decreased, implying related lesions in the organs. The infected mice showed a progressive inflammatory process (Figure 1E). Starting from the accumulation of immune cells predominantly in the perivascular areas at 2 to 4 dpi, immune cells were infiltrated in a larger area of the lung, expanding into the alveolar spaces, with perivascular and interstitial edema at 7 dpi (Figure 1F). In general, the total number of immune cells increased over the course of SARS-CoV-2 infection. The inflammatory cells were mainly composed of a large number of mononuclear cells and fewer neutrophils.

The lung virus burden peaked at 2 dpi and gradually decreased by 7 dpi (Figure 1G). IHC for viral nucleocapsid (N) protein was used to investigate the infection pattern in the lung. The specificity of the antibody used in this study was verified by confirming that two different antibodies showed the same immunofluorescence (IF) stain patterns (Supplemental Figure S2). Viral N protein was widely detected in not only inflammatory areas but also in non-inflamed areas (Figure 1H). Lung tissues at 2 dpi showed a larger positive area and stronger immunoreactivity than lung tissues at 7 dpi (Figure 1H). The infection pattern was also observed in *in situ* hybridization analysis of viral spike protein mRNA (Figure 1I).

Several studies have reported that intranasal inoculation of SARS-CoV-2 into K18-h*ACE2* mice results in a high rate of viral replication in the lungs, followed by spreading to other organs, including the brain.[9–11] Inflammatory reactions were observed in the brain based on the presence of perivascular cuffing by inflammatory cells (Figure 2A), providing evidence of viral invasion into the brain. IHC analyses showed the increased $CD3^+$ T cells and $F4/80^+$ macrophages (Figure 2B). *In situ* hybridization analysis of viral spike protein mRNA revealed viral invasion into the brain (Figure 2C). Viral load and distribution according to the anatomic locations of the brain were investigated on the basis of IHC analyses for viral N protein (Figure 2, D and E). Most infected mice showed a high viral load in the olfactory tubercle, despite the diverse range of viral loads and distribution patterns in the brain (Figure 2D). It has been

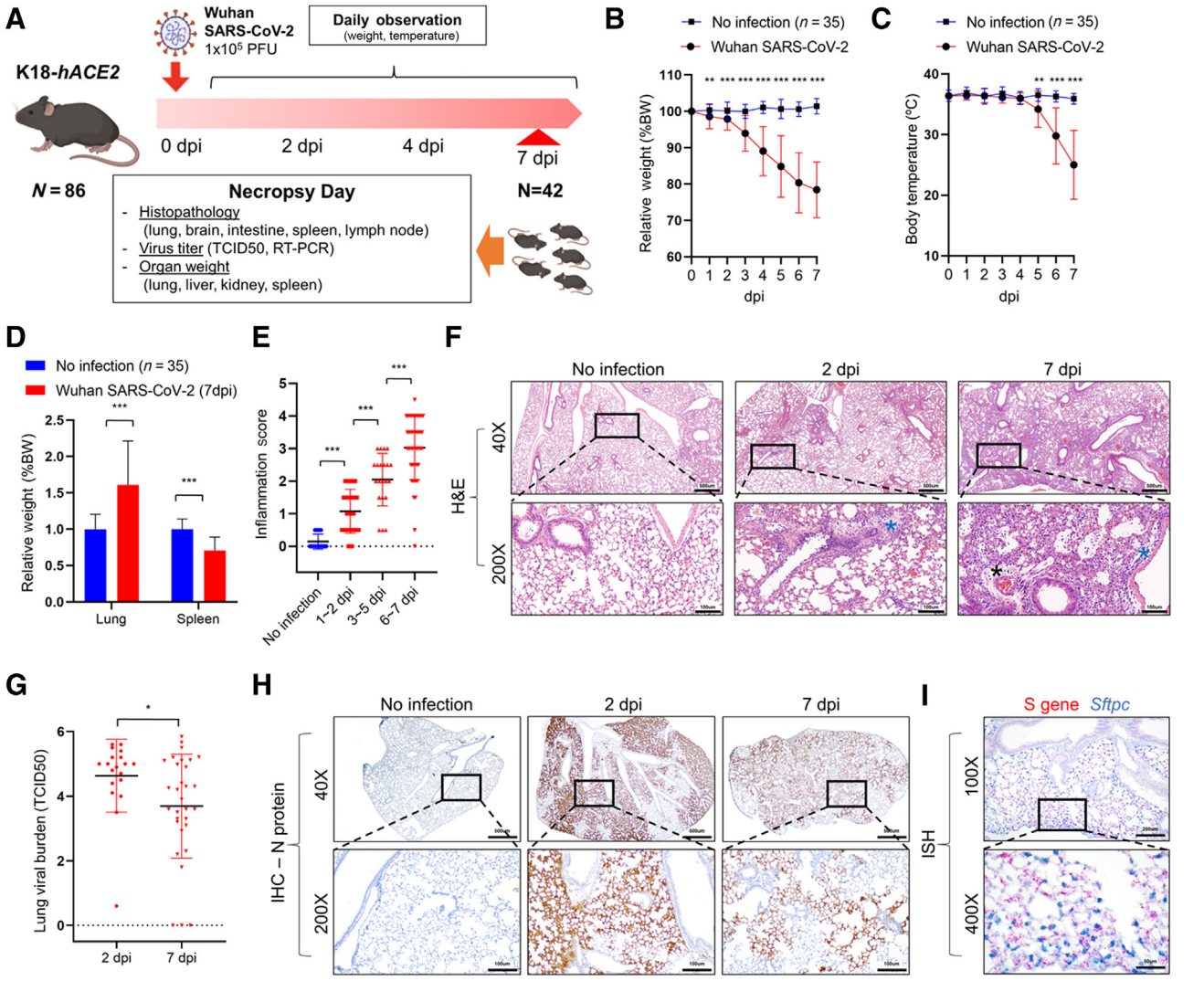

Figure 1 Clinicopathologic characterization of K18-h*ACE2* mice infected with Wuhan SARS-CoV-2. **A:** Eighty-six 8- to 10-week—old male K18-h*ACE2*—transgenic mice were inoculated with 1×10^5 plaque-forming units (PFUs) SARS-CoV-2 via the intranasal route. They were necropsied at 2, 4, and 7 days post infection (dpi). **B:** Weight change of the mice was monitored. Relative body weight (BW), BW at the indicated dpi/BW at 0 dpi (percentage). **C:** Body temperature of the mice was monitored. **D:** Lung and spleen weight of the mice necropsied at 7 dpi was measured. Relative organ weight, organ weight/body weight (percentage). **E:** Histopathologic score of lung inflammation was measured on the basis of hematoxylin and eosin (H&E) slides. **F:** Representative images of H&E staining of lung tissues. **Asterisk** indicates perivascular edema. **Bottom panels:** Magnified images of **boxed areas** (**top panels**). **G:** Viral burden in the lungs was measured at 2 and 7 dpi by 50% tissue culture infectious dose (TCID50). **H:** Representative immunohistochemistry (IHC) images of SARS-CoV-2 nucleocapsid (N) protein in the lungs. **Bottom panels:** Magnified images of **boxed areas** (**top panels**). **I:** Representative *in situ* hybridization (ISH) images of SARS-CoV-2 (red) and Sftpc (green) mRNA of lung tissues. **Bottom panel:** Magnified image of **boxed area** (**top panel**). Error bars indicate means ± SD (**B**—**E** and **G**). $^*P < 0.05$, $^{**}P < 0.01$, and $^{***}P < 0.001$ (*t*-test). Scale bars: 500 μm (×40) (**F** and **H**); 100 μm (×200) (**F** and **H**); 200 μm (×100) (**I**); 50 μm (×400) (**I**).

strongly suggested that SARS-CoV-2 uses the olfactory nerve as a portal for brain infection in human COVID-19 cases.[15] Combined with human evidence, these results support the assumption that SARS-CoV-2 travels along the olfactory nerve from the nose to the brain.

Interestingly, the infected mice commonly developed splenic lesions, including white pulp atrophy, over the course of SARS-CoV-2 infection (Figure 2, F—H). White pulp atrophy was characterized by lymphoid depletion with apoptosis. In human patients, lymphocytopenia is a common characteristic of COVID-19, and its severity levels may serve as a reliable predictive factor for COVID-19 clinical outcomes.[3] Among fatal COVID-19 cases, secondary lymphoid organs, including the spleens and lymph nodes, manifested severe tissue damage and lymphocyte apoptosis.[4] Collectively, this observation suggests that K18-h*ACE2* mice represent a suitable animal model for severe COVID-19 associated with lymphoid depletion.

The spleen acts as a major lymphoid organ regulating immune responses locally and in the whole body and is the main filter for bloodborne pathogens and antigens. This suggests a possibility that SARS-CoV-2 may directly infect lymphocytes via the spread of the virus into the blood, resulting in cell death. To test the possibility, the virus was

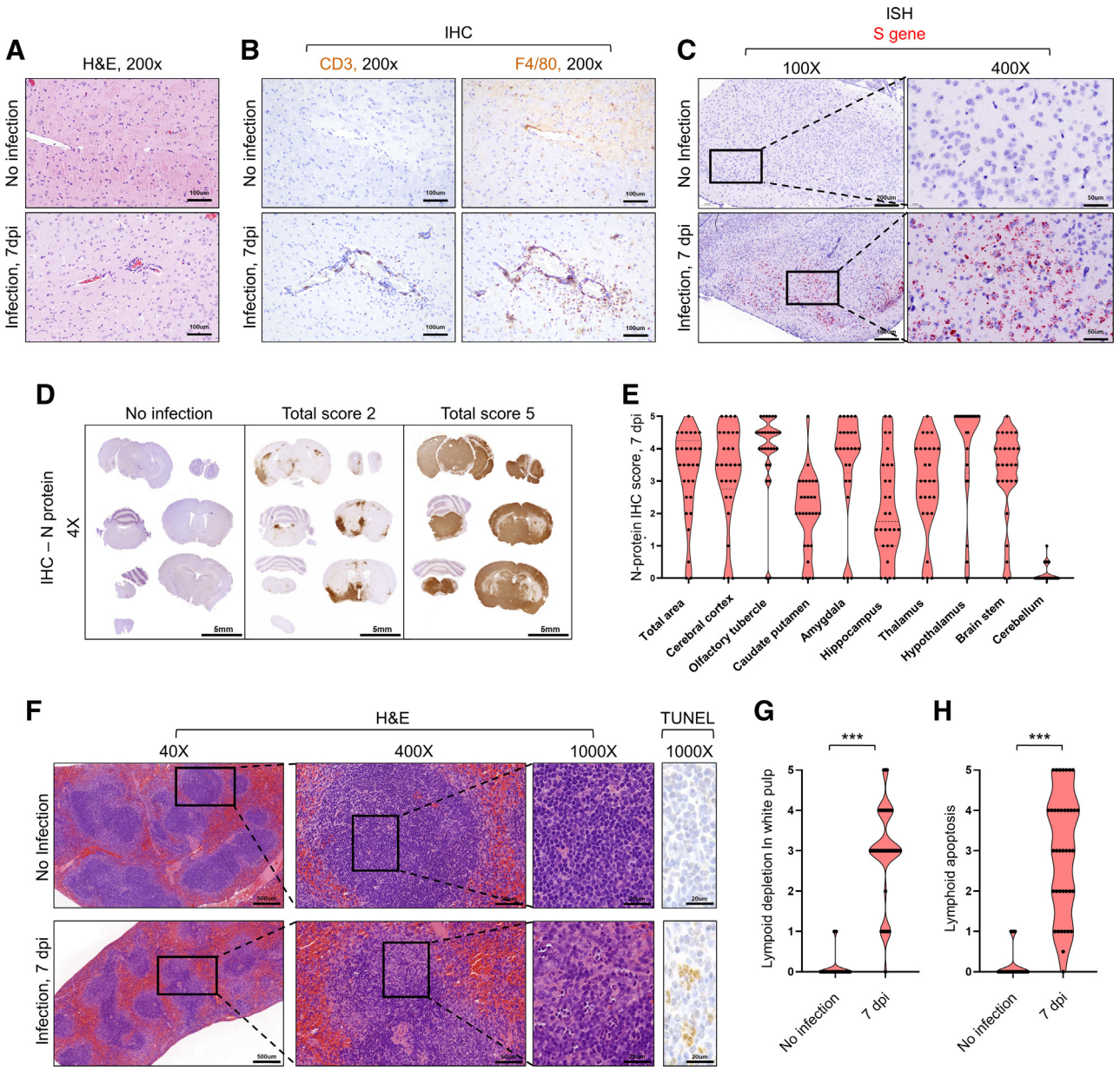

Figure 2 Clinicopathologic characterization of brain of K18-h*ACE2* mice infected with Wuhan SARS-CoV-2. **A:** Representative images of hematoxylin and eosin (H&E) staining of brain tissues. **B:** Representative images of immunohistochemistry (IHC) staining of brain tissues. **C:** Representative *in situ* hybridization (ISH) images of SARS-CoV-2 (red) mRNA of brain tissues. **Right panels:** Magnified images of **boxed areas** (**left panels**). **D:** Representative IHC images of viral nucleocapsid (N) protein in the brain sections according to IHC grade. **E:** Viral N-protein IHC scores according to the anatomic locations of the brain. Scores were measured on the basis of the evaluation of the parenchymal involvement of the viral N-protein–positive area as follows: grade 0, not detectable; grade 1, <10%; grade 2, <25%; grade 3, <50%; grade 4, <75%; and grade 5, >75%. **F:** Representative H&E and terminal deoxynucleotidyl transferase-mediated dUTP nick-end labeling (TUNEL) images of the spleen at 7 dpi. **Boxed areas** are magnified in the **right panels**. **G:** Histologic score of lymphoid depletion in white pulp of the spleen based on H&E slides. **H:** Histologic score of lymphoid apoptosis in white pulp of the spleen based on H&E slides. Error bars indicate means ± SD (**G** and **H**). ***$P < 0.001$ (*t*-test). Scale bars: 100 μm (×200) (**A** and **B**); 200 μm (×100) (**C**); 50 μm (×400) (**C** and **F**); 5 mm (×4) (**D**); 500 μm (×40) (**F**); 20 μm (×1000) (**F**). Dpi, day post infection.

injected through the tail vein (Supplemental Figure S3A). Slight weight loss was observed at 8 dpi (Supplemental Figure S3B), but morphologic changes, such as inflammation and atrophy, were not induced in the lung, spleen, and brain based on hematoxylin and eosin staining (Supplemental Figure S3C). IHC analyses for viral N protein did not show evidence of infection in these organs (Supplemental Figure S3C), indicating that the possibility was low.

Lethality of SARS-CoV-2–Infected Mice Is Characterized by Lymphoid Depletion Associated with Brain Infection

As shown in Figure 1, infected mice showed a diverse range of disease severity in terms of weight, temperature, lung pathology, spleen pathology, and brain infection at 7 dpi. On the basis of these disparities in severity, the correlation

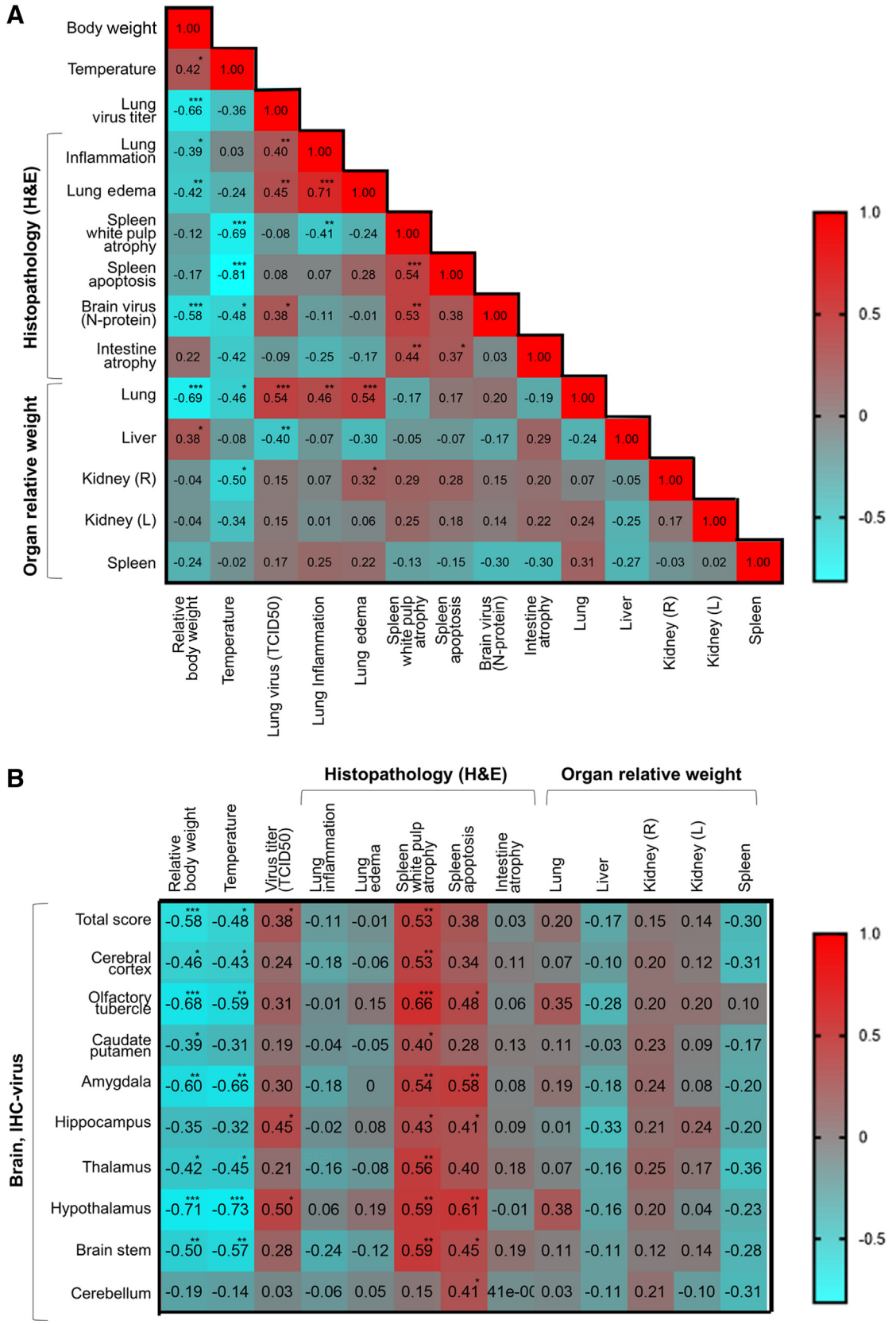

Figure 3 Clinicohistopathologic factors associated with disease severity. **A:** Heat map of Pearson correlation coefficients between disease severity and clinicohistopathologic factors in lymphoid organs. The figure in the box indicates the Pearson *r*. **B:** Heat map of the Pearson correlation coefficients between the brain viral nucleocapsid-protein immunohistochemistry (IHC) grade and disease severity/clinicohistopathologic factors. The figure in the box indicates the Pearson *r*. $*P < 0.05$, $**P < 0.01$, and $***P < 0.001$ (Pearson correlation coefficient test). H&E, hematoxylin and eosin; L, left; R, right; TCID50, 50% tissue culture infectious dose.

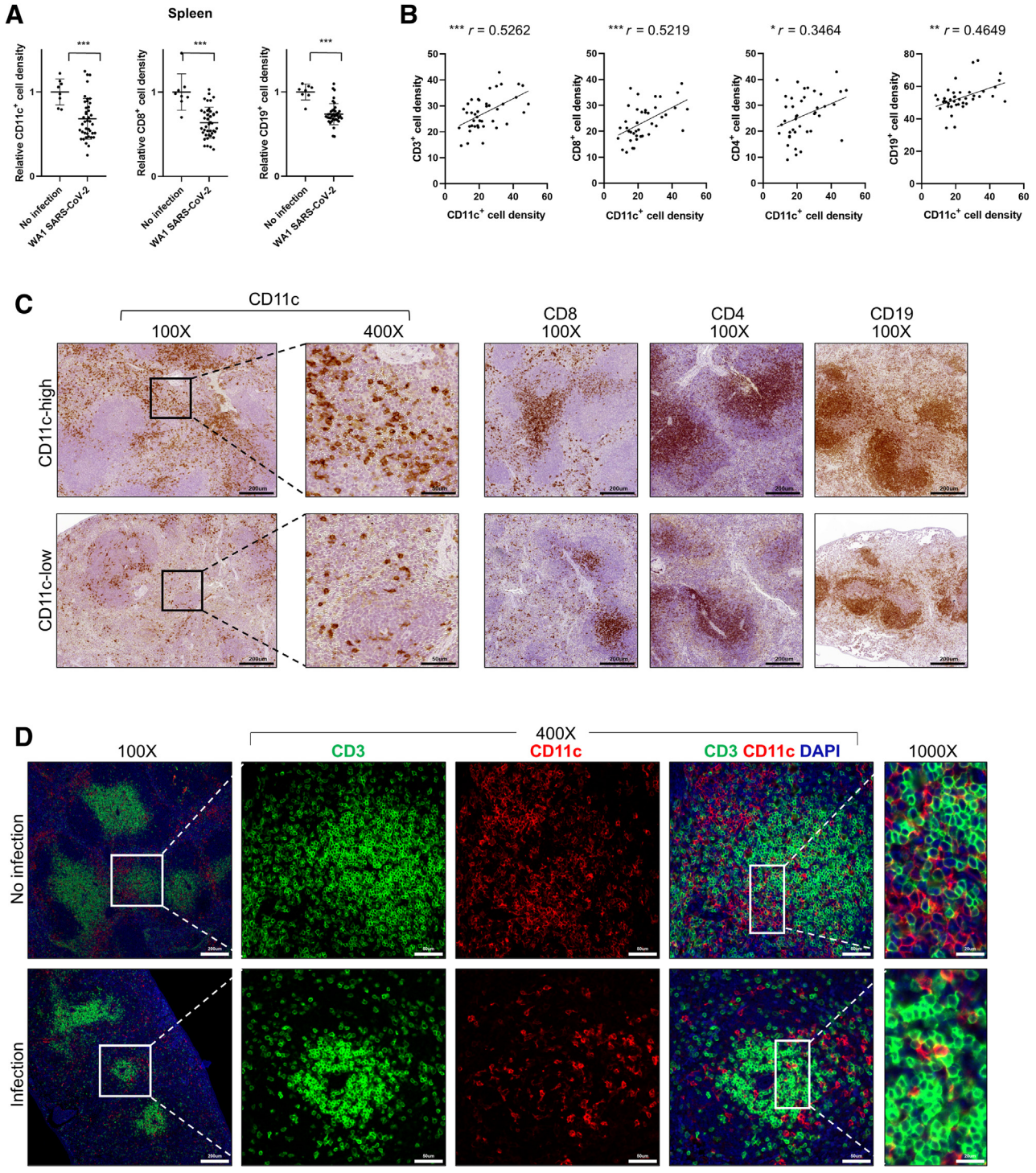

Figure 4 Positive correlation between dendritic cells (DCs) and lymphocytes of Wuhan SARS-CoV-2—infected K18-h*ACE2* mice. **A:** Immunohistochemistry (IHC) analyses of CD11c$^+$ DCs, CD8$^+$ cytotoxic T cells, and CD19$^+$ B cells in the spleen of K18-h*ACE2* mice at 7 days post infection (dpi). The density of immune cell marker—positive cells was calculated by dividing the number of positive cells by the area examined using digital image analysis (Aperio Imagescope). **B:** Correlation between immune cells identified by IHC analysis of immune cell markers in the spleen of K18-h*ACE2* mice at 7 dpi. Pearson correlation test. CD3 indicates pan T cell; and CD4, helper T cell. **C:** Representative IHC images of CD8, CD4, and CD19$^+$ cells in the spleen of K18-h*ACE2* mice at 7 dpi, according to the frequency of CD11c$^+$ cells. **Boxed areas** were magnified in the **right panels**. **D:** Representative immunofluorescence images of CD3$^+$ T cells and CD11c$^+$ DCs in the spleen of K18-h*ACE2* mice at 7 dpi. **Boxed areas** were magnified in the **right panels**. Error bars indicate means ± SD (**A** and **B**). $n = 42$ (**A** and **B**). $^*P < 0.05$, $^{**}P < 0.01$, and $^{***}P < 0.001$ (*t*-test). Scale bars: 200 μm (×100) (**C** and **D**); 50 μm (×400) (**C** and **D**); 20 μm (×1000) (**D**).

between these clinicopathologic parameters was analyzed to define the lethality induced by SARS-CoV-2 infection in the mouse model. Brain viral burden was highly correlated with both body weight loss and a decrease in body temperature (Figure 3A). Given that body weight and temperature are indisputable indicators of lethality in the mouse model, this correlation highlights the lethal consequences of SARS-CoV-2 brain infections in mice. In particular, a high viral load in the hypothalamus was most highly correlated with low body temperature (Figure 3B). As the hypothalamus is the central control of body temperature, its damage could be the cause of the temperature decrease in this mouse model. Thus, these results indicate that, in addition to lung lesions, brain viral load is a major determinant of mortality in this model.

Interestingly, white pulp atrophy in the spleen showed the greatest correlation with brain viral load and body temperature decrease (Figure 3). This finding suggests that lymphoid depletion might be involved in viral invasion and replication in the brain. K18-h*ACE2* mice with high weight loss invariably showed severe splenic lesions and brain infections. Although a mouse lost 13% of its body weight, it did not develop inflammation and viral replication in the lung but manifested splenic lesions and brain infection (Supplemental Figure S4). Altogether, these results highlight the severe lymphoid depletion with apoptosis associated with neuroreplicative potential in the brain as lethal consequences of SARS-CoV-2–infected mice.

Lymphoid Depletion is Associated with Loss of Functionality of Antigen-Presenting Cells Below Basal Levels

To understand the immune dysfunctions in this model, the immune profiles and characteristics of lymphoid organs were examined. IHC analyses of immune cell markers were performed in the spleen and submandibular lymph nodes at 7 dpi (Supplemental Figures S5 and S6). In terms of innate immunity, the $CD11c^+$ dendritic cells (DCs) in the spleens were significantly reduced compared with those in the uninfected spleens (Figure 4A and Supplemental Figures S5 and S6), indicating impaired virus sensing and antiviral immune responses to SARS-CoV-2 infection. In terms of adaptive immunity, the $CD8^+$ cytotoxic T cells and $CD19^+$ B-cell populations in the spleens of the infected mice were significantly reduced compared with those in the uninfected spleens (Supplemental Figure S5). The white pulp of the spleen is mainly composed of T and B cells, which are key players in adaptive immunity. Thus, the white pulp atrophy typically observed in this mouse model could be attributed to a reduction in these cell populations.

On the basis of the analysis of the correlation between these immune cell markers, $CD11c^+$ DCs showed the greatest correlation with $CD8^+$ cytotoxic T cells, $CD4^+$ helper T cells, and $CD19^+$ B cells (Figure 4, B and C, and Supplemental Figure S6). These data raise the possibility that the dysfunction of antigen-presenting cells (APCs), including DCs, causes lymphoid depletion in infected mice. Thus, the physical interaction between DCs and T cells was examined in the spleen (Figure 4D). $CD11c^+$ DCs were clustered and concentrated in the T-cell area in the spleen in the uninfected mice. However, DCs were remarkably reduced and scattered around the T-cell area, indicating the reduced physical interaction between them (Figure 4D).

APCs present antigenic peptides from pathogens in association with MHCII to naïve T lymphocytes and lead to the activation of antigen-specific T cells.[16] To determine the functionality of APCs, MHCII expression in APCs was examined. High-dimensional analysis based on spectral flow cytometry using lung tissues revealed that MHCII expression in the innate immune population deceased over the course of SARS-CoV-2 infection (Figure 5A). Fluorescence-activated cell sorting analysis also showed that $MHCII^+$ DCs in the lung decreased over time during the infection and remarkably decreased at 5 dpi (Figure 5B). On the basis of IF analyses of spleen tissues, the total number of $MHCII^+$ cells of APCs, such as $CD11c^+$ DCs (Figure 5C) and $CD19^+$ B cells (Figure 5D), considerably decreased below the basal level of their uninfected counterparts. Altogether, these data showed that the impaired adaptive immunity showing lymphoid depletion with apoptosis could be attributed to the subnormal level of suppressed APC function induced by SARS-CoV-2 infection.

Lymphoid Depletion with Reduced Dendritic Cells Has Prognostic Value for Disease Severity in SARS-CoV-2 Infection

In the immune cell population, reduced numbers of $CD11c^+$ DCs in the spleen were significantly correlated with disease severity factors, including body weight loss, high lung viral titer, and lung inflammation (Figure 6, A and B, and Supplemental Figure S7). The high brain viral load was highly correlated with reduced numbers of $CD11c^+$ DCs and $CD8^+$ cytotoxic T cells in the secondary lymphoid organs (Figure 6, C and D). These results suggest that the levels of DCs and cytotoxic T cells may serve as reliable predictive factors for outcomes in the preclinical model.

Whether the lethality characterized by lymphoid depletion with the impaired APC/T-cell axis was observed with less pathogenic SARS-CoV-2 variants or with other respiratory viruses, such as influenza A, was tested. The SARS-CoV-2 Omicron variant overwhelms its preceding variants, and in K18-h*ACE2* mice, Omicron causes less severe infection, with low replication levels in the lungs and brains.[17,18] Influenza A is a highly contagious and common respiratory illness that causes seasonal epidemics of the disease known as the flu. K18-h*ACE2* mice were intranasally infected with 1×10^5 PFUs of Wuhan, Delta, and Omicron of SARS-CoV-2, or 1×10^2 PFUs of

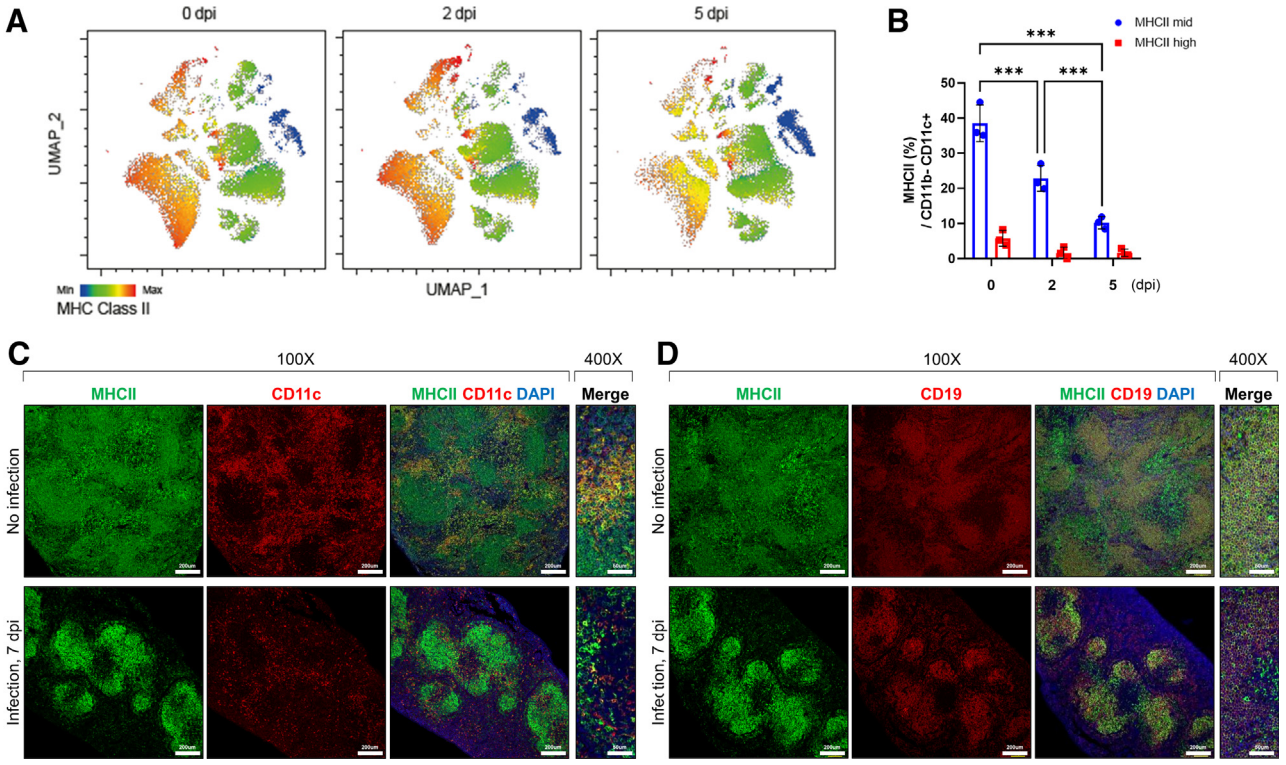

Figure 5 Analyses of major histocompatibility complex class II (MHCII) expression in the lung and spleen of K18-h*ACE2* mice infected with Wuhan SARS-CoV-2. **A:** High-dimensional analysis of spectral flow cytometry data of MHCII on nine markers for immune population (CD3, CD11b, CD11c, CD19, CD45, LY6c, LY6g, F4/80, and sialic acid-binding immunoglobulin-like lectin F (SIGLEC-F) from the lung of male K18-h*ACE2* mice before or after SARS-CoV-2 infection using Flow Jo software version 10. Visual stochastic network embedding (viSNE) maps were fed into the FlowSOM clustering algorithm. **B:** Fluorescence-activated cell sorting analysis using lung tissues to examine MHCII$^+$ dendritic cells (DCs) at the indicated day post infection (dpi). **C** and **D:** Immunofluorescence analysis using spleen tissues to examine MHCII expression in antigen-presenting cells, including CD11c$^+$ DCs (**C**) and CD19$^+$ B cells (**D**). Error bars indicate means ± SD (**B**). $n = 3$ at each time point (**B**). ***$P < 0.001$ (*t*-test). Scale bars: 200 μm (×100) (**C** and **D**); 50 μm (×400) (**C** and **D**).

influenza A (Figure 7A). At the indicated infection dose, SARS-CoV-2 Omicron did not cause a fatal weight loss (>25%) or body temperature decrease (<30°C) (Figure 7, B and C). Omicron induced lower levels of viral replication in the lungs compared with Wuhan at 7 dpi (Figure 7D). On the basis of hematoxylin and eosin analysis, SARS-CoV-2 Omicron showed a low trend in lung inflammation, but with no statistical significance compared with Wuhan and Delta (Figure 7, E and F). Interestingly, a much less severe lymphoid depletion in the spleen was observed at 7 dpi with Omicron than with Wuhan and Delta (Figure 7, G and H). Only two mice (40%) developed mild to moderate lymphoid depletion and exhibited relatively greater weight loss and lower body temperature than the other Omicron-infected mice without lymphoid depletion. IHC analyses showed that sufficient MHCII$^+$ cells, CD11c$^+$ DCs, and CD3$^+$ T cells were present in the spleens of Omicron-infected mice, but not in Wuhan-infected mice (Figure 7I). These results suggest that the severity of lymphoid depletion is an important indicator of lethality among SARS-CoV-2 strains.

Influenza A virus induced weight loss and a decreased body temperature similar to that observed with Wuhan SARS-CoV-2, which could be defined as lethality until 7 dpi (Figure 7, B and C). Influenza A virus infection promoted a similar level of lung inflammation to that seen with Wuhan (Figure 7, E and F), but did not cause lymphoid depletion in the spleen (Figure 7, G and H). On the basis of IHC analyses, the MHCII$^+$, CD11c$^+$ DCs, and CD3$^+$ T cells were strongly preserved in the spleens of influenza A–infected mice (Figure 7I). These data suggest that lymphoid depletion, together with the impaired APC/T-cell axis, is a specific feature of SARS-CoV-2 infection and has prognostic value for predicting disease severity in SARS-CoV-2 infection.

h*ACE2* Expression Patterns Determine Lethality Exhibiting Lymphoid Depletion in Part through a Defective Stimulator of Interferon Genes Pathway

As virus tissue distribution, such as brain infection, could be a determinant of lethality based on the present findings (Figure 2), a CAG-h*ACE2* mouse model robustly expressing h*ACE2* in most types of cells was established to investigate virus cellular tropism in the previous study.[11] The K18 promoter is active mainly in the glandular and respiratory

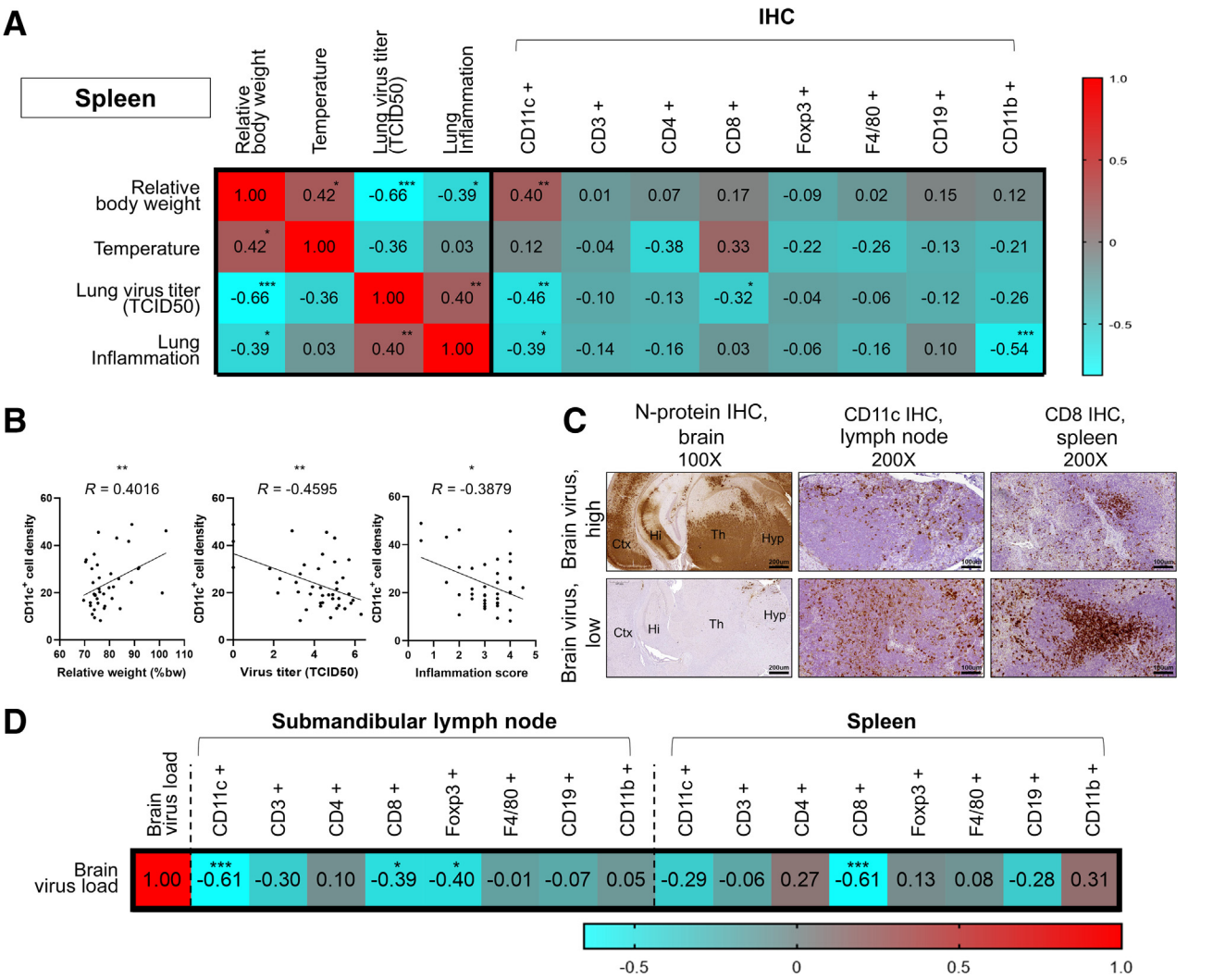

Figure 6 Clinicohistopathologic factors associated with immune cell marker density in K18-h*ACE2* mice infected with Wuhan SARS-CoV-2 at 7 days post infection (dpi). **A:** Heat map of Pearson correlation coefficients between disease severity and immune cell marker density from immunohistochemistry (IHC) digital analysis in spleen of K18-h*ACE2* mice at 7 dpi. The figure in the box indicates the Pearson *r*. **B:** The density of $CD11c^+$ cells significantly correlated with severity factors. **C:** Representative IHC images of $CD11c^+$ cells in the lymph node and $CD8^+$ cells in the spleen according to the brain viral burden based on the viral nucleocapsid (N) protein IHC analysis. **D:** Heat map of the Pearson correlation coefficients between the brain viral N-protein IHC grade and the density of immune cell markers in the lymphoid organs at 7 dpi. The figure in the box indicates the Pearson *r*. $*P < 0.05$, $**P < 0.01$, and $***P < 0.001$ (Pearson correlation coefficient test). Scale bars: 200 μm (×100) (**C**); 100 μm (×200) (**C**). Ctx, cerebral cortex; Hi, hippocampus; Hyp, hypothalamus; TCID50, 50% tissue culture infectious dose; Th, thalamus.

epithelium of the lung,[19] whereas the CAG promoter is a ubiquitously active and strong promoter in mammalian cells. On the basis of IHC analyses, K18-h*ACE2*-FVB expressed h*ACE2* mainly in respiratory epithelium, including bronchiolar epithelial cells and alveolar cells, whereas CAG-h*ACE2*-FVB mice exhibited much higher expression of h*ACE2* in most lung cells than K18-h*ACE2*-FVB mice (Figure 8A). K18-h*ACE2*-FVB mice or CAG-h*ACE2*-FVB mice were intranasally infected with 1×10^5 PFUs of SARS-CoV-2 and followed up until 7 dpi (Figure 8B). K18-h*ACE2*-FVB mice experienced a weight loss of >25% (Figure 8C), exhibited decreased body temperature, and became moribund, like K18-h*ACE2* mice, in C57BL/6 strain. However, CAG-h*ACE2*-FVB mice did not show significant weight loss and activity, which could be defined as lethality (Figure 8C). Between these two models, there were no significant differences in lung lesions, such as histopathologic inflammation scores and virus titers (Figure 8, D and E). On the basis of IF analyses, these models showed similar virus infection patterns (Supplemental Figure S8). $PDPN^+$ type I pneumocytes were the main infected cells in both models. Neither model showed detectable viral infection with immunostaining in the endothelial cells of vessels and DCs. Collectively, these findings indicate that h*ACE2* levels and patterns might determine lethality without altering viral cell tropism.

CAG-h*ACE2* mice did not show splenic lesions in the histopathologic findings (Figure 8F). In addition, virus

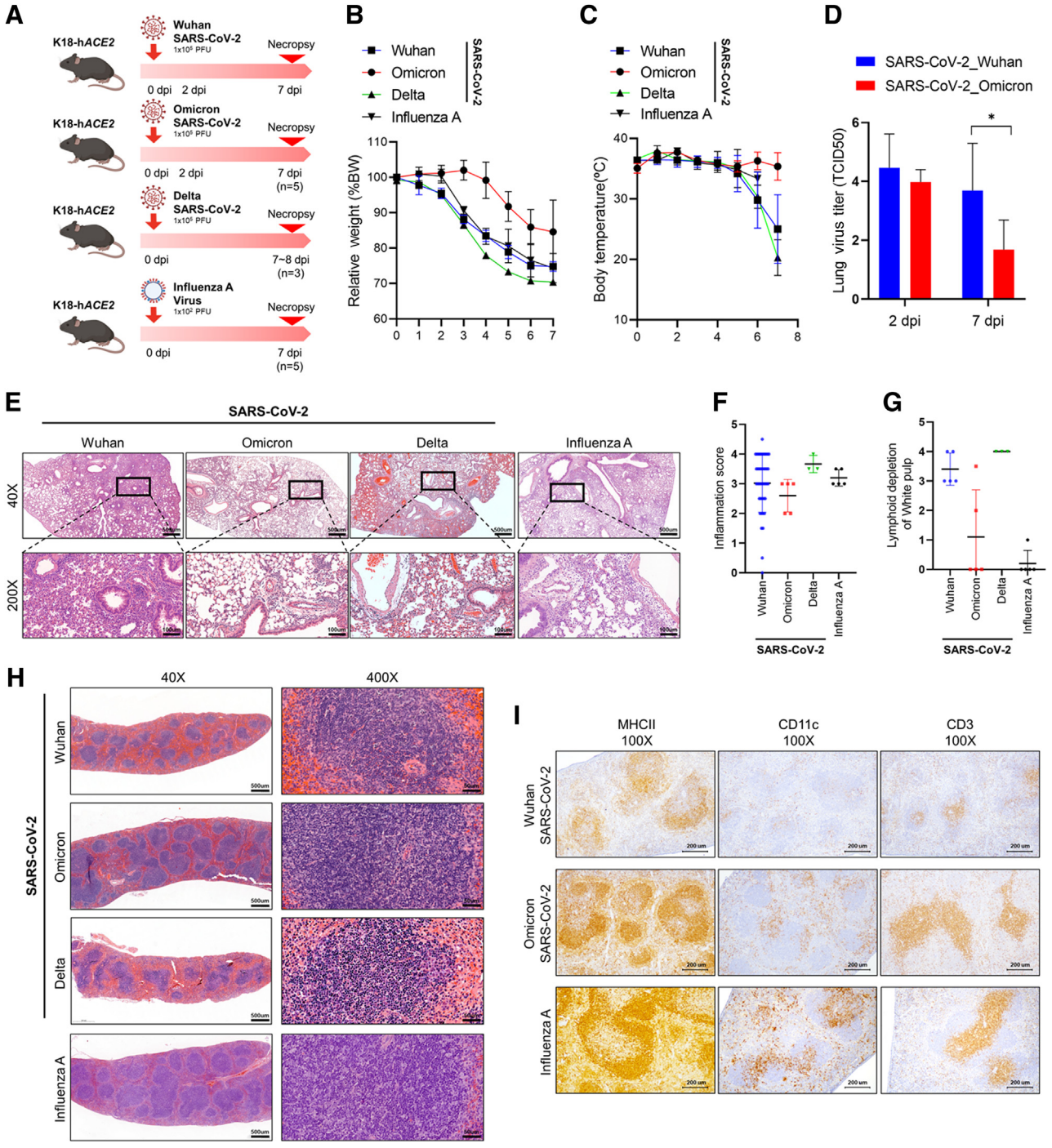

Figure 7 Clinicopathologic characteristics of K18-h*ACE2* mice infected with Wuhan SARS-CoV-2, SARS-CoV-2 Omicron variant, SARS-CoV-2 Delta variant, and influenza A. **A:** The 8- to 10-week—old male K18-h*ACE2*-transgenic mice were inoculated with 1×10^5 plaque-forming units (PFUs) Wuhan SARS-CoV-2, 1×10^5 PFUs SARS-CoV-2 Omicron variant, 1×10^5 PFUs SARS-CoV-2 Delta variant, and 1×10^2 PFUs influenza A via the intranasal route. **B:** Weight change of the mice was monitored daily. **C:** Body temperature of the mice was monitored daily. **D:** Viral burden in the lungs was measured at 2 and 7 days post infection (dpi) by 50% tissue culture infectious dose (TCID50). **E:** Representative images of hematoxylin and eosin (H&E) staining of lung tissues at 7 dpi. **Bottom panels:** Magnified images of **boxed areas** (**top panels**). **F:** Histopathologic score of lung inflammation at 7 dpi was measured on the basis of H&E slides. **G:** Histologic score of lymphoid depletion in white pulp of the spleen at 7 dpi based on H&E slides. **H:** Representative H&E images of spleen tissues at 7 dpi. **Right panels:** High-power images. **I:** Representative immunohistochemistry images for major histocompatibility complex class II (MHCII), CD11c, and $CD3^+$ cells in the spleen at 7 dpi. Error bars indicate means ± SD (**B**—**D**, **F**, and **G**). $n = 5$ mice inoculated with 1×10^5 PFUs SARS-CoV-2 Omicron variant and mice inoculated with 1×10^2 PFUs influenza A (**A**); $n = 3$ mice inoculated with 1×10^5 PFUs SARS-CoV-2 Delta variant (**A**). $^*P < 0.05$ (*t*-test). Scale bars: 500 μm (×40) (**E** and **H**); 100 μm (×200) (**E**); 50 μm (×400) (**H**); 200 μm (×100) (**I**).

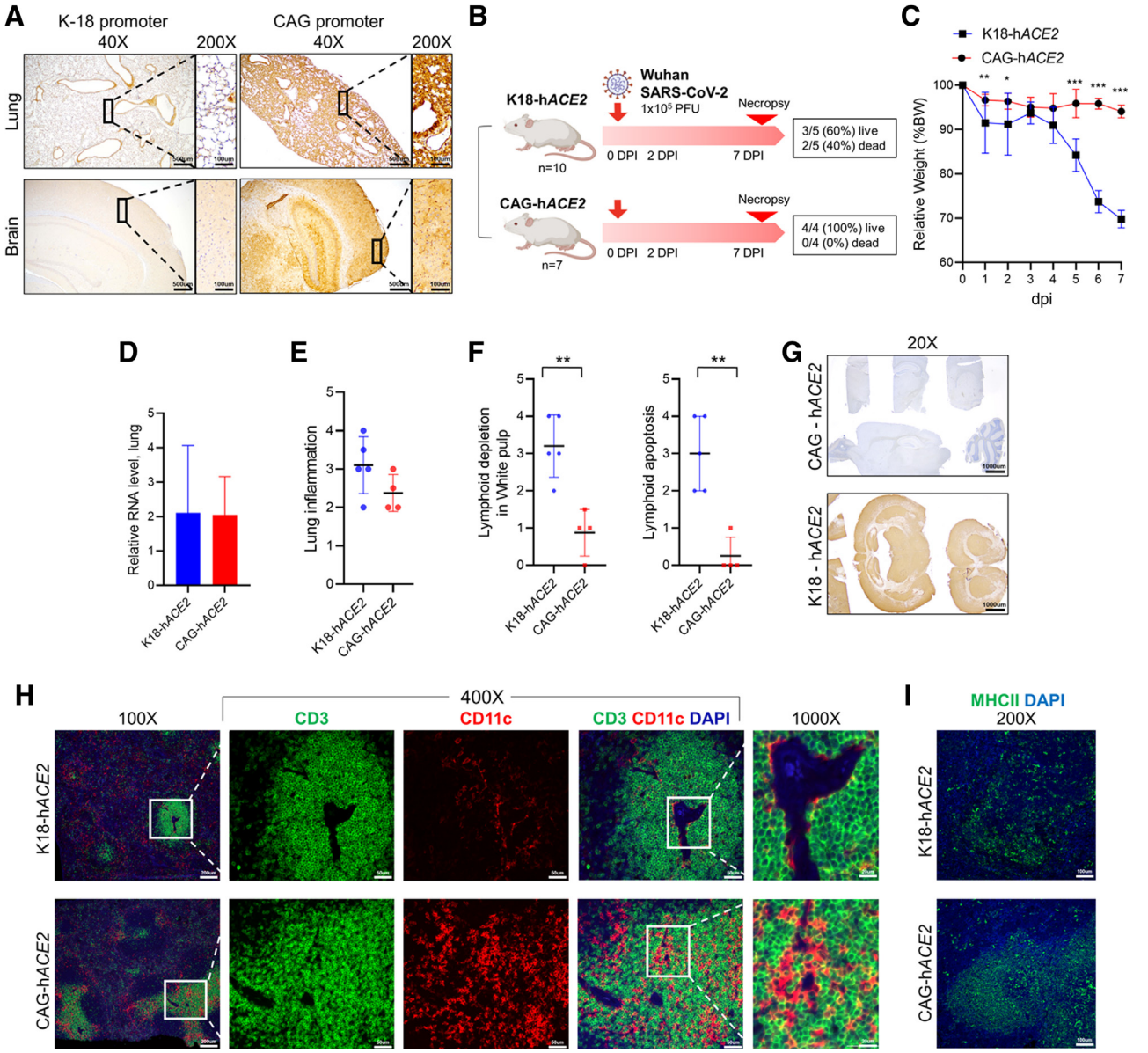

Figure 8 Comparison of clinicopathologic characteristics between K18-hACE2 and CAG-h*ACE2* mice infected with Wuhan SARS-CoV-2. **A:** Immunohistochemistry (IHC) images of h*ACE2* protein in the lung and brain of K18-h*ACE2*-FVB and CAG-h*ACE2*-FVB mice. **Boxed areas** were magnified in the **right panels**. **B:** K18-h*ACE2* and CAG-h*ACE2* mice were inoculated with 1×10^5 plaque-forming units Wuhan SARS-CoV-2 via the intranasal route. **C:** Relative body weight changes were monitored daily in the mice after the infection. **D:** Viral burden in the lung was measured at 7 days post infection (dpi) by RT-PCR analysis. **E:** Histopathologic lung inflammation score of K18-h*ACE2* and CAG-h*ACE2* mice at 7 dpi. **F:** Histologic score of lymphoid depletion and apoptosis in white pulp of the spleen based on hematoxylin and eosin slides. **G:** IHC images of viral nucleocapsid (N) protein in the brain of K18-h*ACE2*-FVB and CAG-h*ACE2*-FVB mice at 7 dpi. **H:** Representative immunofluorescence (IF) images of $CD3^+$ T cells and $CD11c^+$ dendritic cells in the spleen of K18-hACE2-FVB and CAG-h*ACE2*-FVB mice at 7 dpi. CD3, green; and CD11c, red. **Boxed areas** were magnified in the **right panels**. **I:** IF images of major histocompatibility complex class II (MHCII) in the spleen of K18-h*ACE2*-FVB and CAG-h*ACE2*-FVB mice at 7 dpi. Error bars indicate means ± SD (**C**–**F**). $*P < 0.05$, $**P < 0.01$, and $***P < 0.001$ (*t*-test). Scale bars: 500 μm (×40) (**A**); 100 μm (×200) (**A** and **I**); 1000 μm (×20) (**G**); 200 μm (×100) (**H**); 50 μm (×400) (**H**); 20 μm (×1000) (**H**).

invasion into the brain was not observed in CAG-h*ACE2* mice, except for one mouse showing mild focal positivity for viral N protein (Figure 8G). On the basis of IF analyses, $CD11c^+$ DCs and CD3 T cells were well preserved and physically interacted with each other in CAG-h*ACE2* mice (Figure 8H). The number of $MHCII^+$ cells was much higher in the spleen of infected CAG-h*ACE2* mice than in K18-h*ACE2* mice (Figure 8I). The number of $MHCII^+$ cells was also higher in the lung of infected CAG-h*ACE2* mice than in K18-h*ACE2* mice (Figure 9, A and B). The proportion of $MHCII^+$ cells in alveolar type II cells or DCs was significantly higher in the lungs of CAG-h*ACE2* mice than in K18-h*ACE2* mice (Figure 9, C and D). $MHCII^+$ cells were mainly composed of $SP\text{-}C^+$ alveolar type II cells and $CD11c^+$ DCs in the lung of infected CAG-h*ACE2* mice (Figure 9E). Alveolar type II cells are known to express

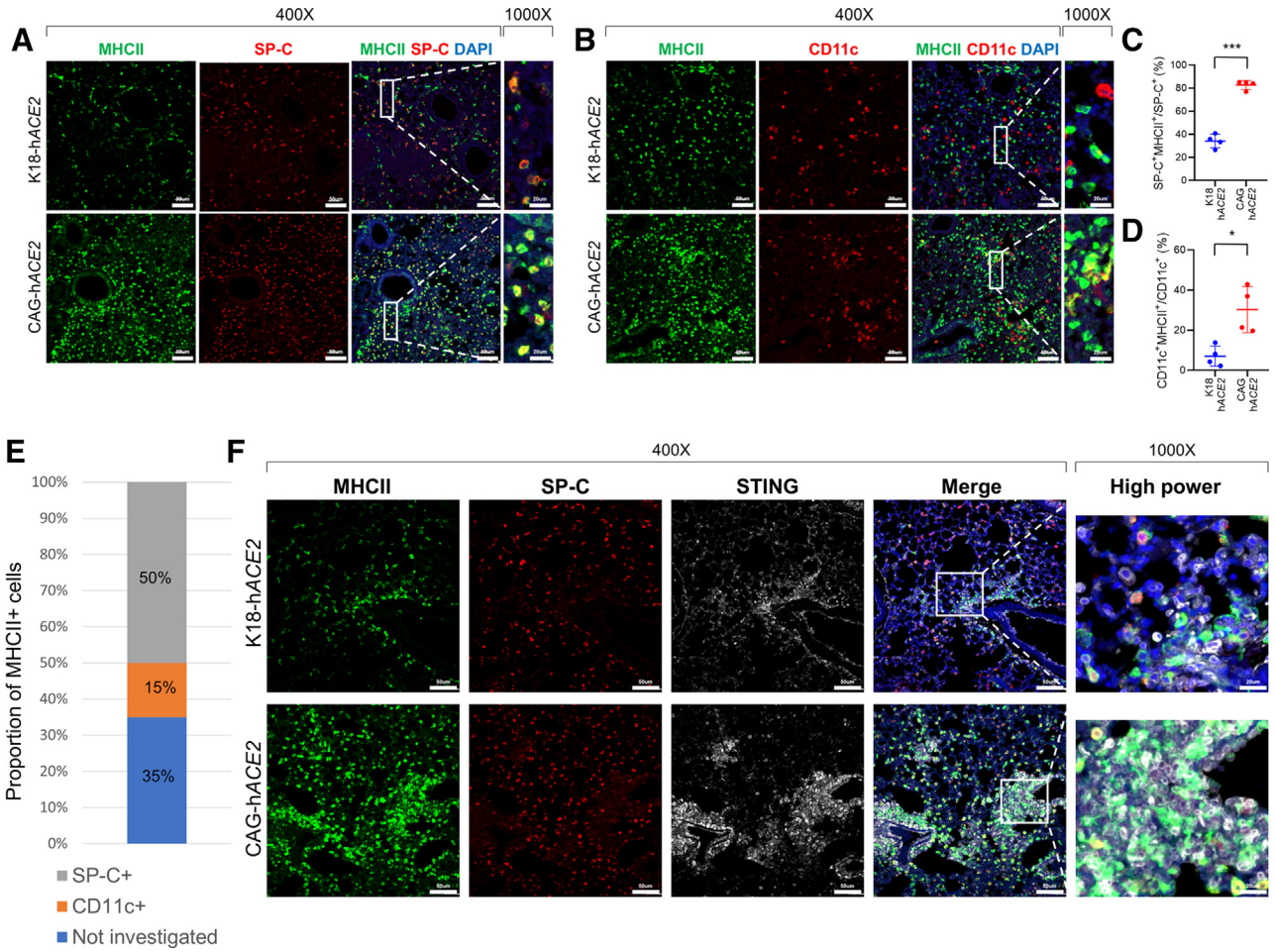

Figure 9 Major histocompatibility complex (MHC) and stimulator of interferon genes (STING) expression in the lung and spleen of K18-h*ACE2* and CAG-h*ACE2* mice at 7 days post infection (dpi). **A:** Representative immunofluorescence (IF) staining images for MHC class II (MHCII; green), surfactant protein C (SP-C) [red; alveolar type II (AT2) cells], and nuclei marker DAPI (blue) in the lung of K18-h*ACE2* and CAG-h*ACE2* mice at 7 dpi. **Boxed areas** were magnified in the **right panels**. **B:** Representative IF staining images for MHCII (green), CD11c [red; dendritic cells (DCs)], and nuclei marker DAPI (blue) in the lung of K18-h*ACE2* and CAG-h*ACE2* mice at 7 dpi. **Boxed areas** were magnified in the **right panels**. **C:** The percentage of MHC^+ cells in $SP\text{-}C^+$ AT2 cells of the lung of K18-h*ACE2* and CAG-h*ACE2* mice. **D:** The percentage of MHC^+ cells in $CD11c^+$ DCs of the lung of K18-h*ACE2* and CAG-h*ACE2* mice. **E:** Proportion of $MHCII^+$ cell types in the lung of CAG-h*ACE2*-FVB mice at 7 dpi. **F:** Representative IF staining images for MHCII (green), SP-C (red; AT2 cells), STING (white), and nuclei marker DAPI (blue) in the lung of K18-h*ACE2* and CAG-h*ACE2* mice at 7 dpi. **Boxed areas** were magnified in the **right panels**. Error bars indicate means ± SD (**C** and **D**). $*P < 0.05$, $***P < 0.001$ (*t*-test). Scale bars: 50 μm (×400) (**A**, **B**, and **F**); 20 μm (×1000) (**A**, **B**, and **F**).

MHCII molecules, which improve respiratory viral disease outcomes.[20]

The cytokine interferon-γ (IFN-γ) can induce MHCII in many different cell types, leading to antigen presentation to T cells and immune activation.[21,22] To examine IFN responses in the lung, the authors investigated the expression of the stimulator of interferon genes (STING), which is activated by cytosolic DNA released from mitochondria or nuclei due to cellular stress during virus infection and is a critical driver of STING-dependent type I IFN signature.[23–25] The STING pathway can be activated in COVID-19 and play an important role in protecting the host from infection.[24,25] More importantly, IF analysis showed significant up-regulation of STING in the lung of CAG-h*ACE2* mice model compared with K18-h*ACE2* mice (Figure 9F). $MHCII^+$ cells are concentrated in $STING^+$ regions, and many of them overlapped with $STING^+$ cells in the infected mice (Figure 9F). $MHCII^+$ $SP\text{-}C^+$ cells did not express STING, suggesting that MHCII expression in alveolar type II cells may be induced in a paracrine manner by IFN from $STING^+$ immune cells. These data show that ineffective STING-controlled immune signaling in host defense against viral invasion may fail to regulate MHCII expression in the lethal model. Collectively, the authors found significant differences in MHCII expression of APCs between mouse models susceptible and resistant to SARS-CoV-2 infection, which may confer an appreciable advantage in overall disease outcomes after SARS-CoV-2 infection.

Discussion

Clinically, the disease severity of COVID-19 varies and is highly linked to the lymphoid depletion,[3–6] but the

mechanisms involved remain elusive. In this study, h*ACE2* transgenic mouse models susceptible to SARS-CoV-2 were used to investigate the characteristics and determinants of lethality associated with the lymphoid depletion specifically observed in SARS-CoV-2 infection. Methodologically, the in-depth comparative study was performed using mouse models and SARS-CoV-2 strains exhibiting different lethality. This study provides unbiased results by analyzing the correlation between clinicohistopathologic and immunologic data using a large number of mice under identical infectious conditions and genetic backgrounds. Lymphoid depletion might be attributed to a suppressed functionality of APCs below basal levels. Lymphoid depletion with reduced APC function was a specific feature observed in SARS-CoV-2 infection and has the greatest prognostic value for disease severity in rodent models and SARS-CoV-2 variants. The data also provide evidence that suppressed APC function could be determined by the h*ACE2* expression pattern and interferon-related signaling. Collectively, these findings demonstrated that lymphoid depletion associated with impaired APC function characterizes lethality in COVID-19 mouse models.

T-cell depletion in lymphoid tissues, which are also associated with apoptosis and lymphocytopenia, has been associated with poor disease outcomes in patients with COVID-19.[5,6] The mechanisms involved are still elusive, but different hypotheses have been raised. The main explanation is that this is due to cytokine storm and secreting factors, which could induce apoptosis of lymphoid cells. A study suggested that T cells expressing Fas/CD95 are more likely to die due to high levels of plasma FasL, which are correlated with CXCL10.[6] Immune suppressive cytokines induced by SARS-CoV-2 infection, including transforming growth factor-β and IL-10, could also induce lymphoid depletion and apoptosis. The pathogenesis of COVID-19 by cytokine storms has been proposed to be a consequence of the disequilibrated cytokine network resulting from the increased biological activity of transforming growth factor-β.[26] In addition, T cells exhibit exhaustion phenotypes with the expression of higher levels of exhaustion markers, including programmed cell death protein 1 (PD-1), which may be induced by cytokine storm.[27] Second, SARS-CoV-2 may directly infect lymphoid cells, resulting in cell death. However, the possibility could be excluded because there was no infection of lymphoid cells even through direct inoculation of virus via vessels.

Interestingly, this study provides unique insight into the impaired adaptive immunity that likely results from the impaired functionality of APCs for maturation and T-cell activation against SARS-CoV-2. These results showed that the heterogeneity in disease manifestations and severity of COVID-19 mouse models is due to variable degrees of impairment in the innate immune mechanisms of APCs. Consequently, a lack of timely developed CD8 T-cell responses could contribute to disease severity during acute SARS-CoV-2 infection. In human cases, accumulating evidence now suggests that the remarkable heterogeneity in COVID-19 manifestations has been linked to defective innate immune responses.[28] The overall reduction of MHCII in APCs, including DCs, raises the possibility that a global dysfunction of APCs may result from defective IFN responses in the lethal models. Indeed, reduced IFN signals were observed in the lethal model. A human study performed single-cell RNA sequencing of blood APCs in 15 patients with moderate or severe COVID-19 pneumonia and found multiprocess defects in antiviral immune defense in specific APCs from patients with severe disease.[29] The IFN pathway was defective in APCs of severe COVID-19 cases. Collectively, these results suggest a global perturbation of IFN downstream functions in severe COVID-19 APCs. Because significantly reduced DCs were found, it is expected that viruses would have developed ways to target these cells and/or interfere with their functions. However, no evidence of direct infection of DCs was found. Further studies are needed to elucidate the mechanism of reduced IFN and impaired APC functionality. Ultimately, this study may form the groundwork for novel therapies to restore defective APC functions in patients with COVID-19.

Unexpectedly, CAG-h*ACE2* mice showing ubiquitous and robust expression of h*ACE2* exhibited favorable outcomes against SARS-CoV-2 infection. This could be attributed to the fact that multiple host molecules, in addition to h*ACE2*, are required for the viral entry of SARS-CoV-2.[30] It is expected that host target cells of SARS-CoV-2 sufficiently possess these factors to ensure efficient viral entry, but most cell types do not. This explanation could be supported by the finding that this model did not show the changed virus cellular tropism in CAG-h*ACE2* mice in comparison with the K18-h*ACE2* model. As most cell types lacking other molecules required for viral entry have a strong expression of h*ACE2* in CAG-h*ACE2* mice, they may trap the virus and cause virus neutralization. It is expected that APCs also efficiently capture the viral antigen and display them to adaptive immune cells for timely CD8 T-cell responses in the CAG-h*ACE2* COVID-19 model. Another explanation is attributed to the physiological roles of h*ACE2* as a key counter regulator of the renin-angiotensin system.[31] *ACE2* is an enzyme that produces angiotensin 1,7 from angiotensin II. High levels of *ACE2* lead to a high angiotensin 1,7 level, which exerts some protective actions against detrimental inflammation.[32] Indeed, *ACE2* protected animals from lung diseases in several viral infection models, such as influenza and respiratory syncytial virus.[33,34] The efficiency of MHCII antigen presentation is altered by *ACE* overexpression.[35] In this context, it has been suggested that the loss of *ACE2* activity induced by viral invasion may be especially detrimental in people with baseline *ACE2* deficiency.[36] In light of these studies, our mouse data suggest that h*ACE2* might be considered a prognostic factor that determines the outcomes of patients with COVID-19.

The Omicron variant is more transmissible and less pathogenic than previous strains of SARS-CoV-2, but the mechanisms of reduced virulence remain to be elucidated. This study suggests that the reduced virulence of Omicron could be attributed to attenuated lymphoid depletion and that Omicron somehow adopted this as an advantage as they evolved. Collectively, our data support that the intrinsic severity of the SARS-CoV-2 strains might depend on the severity of lymphoid depletion. Thus, elucidating the mechanism of lymphoid depletion would provide clues on how to modulate the virulence of SARS-CoV-2. This is the first study to focus on APC functionality in relation to the lymphoid depletion and lethality. The findings of the current study will pave the way for future investigations of how reduced APC function may cause lymphocyte depletion in the inflammatory and exhausted environment induced by SARS-CoV-2 infection. In conclusion, our work revealed that murine COVID-19 lethality is characterized by lymphoid depletion. Our in-depth and comprehensive understanding of COVID-19 mouse models also suggests a potential therapeutic approach to prevent severe progression of COVID-19 by enhancing APC functionality.

Acknowledgment

We thank the Korea Basic Science Institute National Research Facilities and Equipment Center for assistance.

Author Contributions

Y.J.L., S.H.S., and N.Y.L. performed immunohistochemistry, analyzed data, and wrote the manuscript; H.J.Cho., Y.W.L., H.J.Cha., J.-Y.H., and S.-B.L. performed animal experiments and *in vitro* assays; D.I.O., H.A.N., J.-W.Y., J.-S.S., J.-Y.S., H.-K.K., K.T.N., and H.L. curated data and provided resources; and H.Y.L., J.W.P., and J.K.S. supervised the study.

Supplemental Data

Supplemental material for this article can be found at *http://doi.org/10.1016/j.ajpath. 2023.03.008*.

References

1. Stein SR, Ramelli SC, Grazioli A, Chung JY, Singh M, Yinda CK, Winkler CW, Sun J, Dickey JM, Ylaya K, Ko SH, Platt AP, Burbelo PD, Quezado M, Pittaluga S, Purcell M, Munster VJ, Belinky F, Ramos-Benitez MJ, Boritz EA, Lach IA, Herr DL, Rabin J, Saharia KK, Madathil RJ, Tabatabai A, Soherwardi S, McCurdy MT; NIH COVID-19 Autopsy Consortium, Peterson KE, Cohen JI, de Wit E, Vannella KM, Hewitt SM, Kleiner DE, Chertow DS: SARS-CoV-2 infection and persistence throughout the human body and brain. Nature 2022, 612:758–763
2. Garcia-Gonzalez P, Tempio F, Fuentes C, Merino C, Vargas L, Simon V, Ramirez-Pereira M, Rojas V, Tobar E, Landskron G, Araya JP, Navarrete M, Bastias C, Tordecilla R, Varas MA, Maturana P, Marcoleta AE, Allende ML, Naves R, Hermoso MA, Salazar-Onfray F, Lopez M, Bono MR, Osorio F: Dysregulated immune responses in COVID-19 patients correlating with disease severity and invasive oxygen requirements. Front Immunol 2021, 12:769059
3. Lee J, Park SS, Kim TY, Lee DG, Kim DW: Lymphopenia as a biological predictor of outcomes in COVID-19 patients: a nationwide cohort study. Cancers (Basel) 2021, 13:471
4. Xiang Q, Feng Z, Diao B, Tu C, Qiao Q, Yang H, Zhang Y, Wang G, Wang H, Wang C, Liu L, Wang C, Liu L, Chen R, Wu Y, Chen Y: SARS-CoV-2 induces lymphocytopenia by promoting inflammation and decimates secondary lymphoid organs. Front Immunol 2021, 12:661052
5. Kaneko N, Kuo HH, Boucau J, Farmer JR, Allard-Chamard H, Mahajan VS, et al: Loss of Bcl-6-expressing T follicular helper cells and germinal centers in COVID-19. Cell 2020, 183:143–157.e13
6. Andre S, Picard M, Cezar R, Roux-Dalvai F, Alleaume-Butaux A, Soundaramourty C, Cruz AS, Mendes-Frias A, Gotti C, Leclercq M, Nicolas A, Tauzin A, Carvalho A, Capela C, Pedrosa J, Castro AG, Kundura L, Loubet P, Sotto A, Muller L, Lefrant JY, Roger C, Claret PG, Duvnjak S, Tran TA, Racine G, Zghidi-Abouzid O, Nioche P, Silvestre R, Droit A, Mammano F, Corbeau P, Estaquier J: T cell apoptosis characterizes severe Covid-19 disease. Cell Death Differ 2022, 29:1486–1499
7. Xia Y, Hu G, Chen Y, Yuan J, Zhang J, Wang S, Li Q, Wang Y, Deng Z: Embryonic stem cell derived small extracellular vesicles modulate regulatory T cells to protect against ischemic stroke. ACS Nano 2021, 15:7370–7385
8. Hoffmann M, Kleine-Weber H, Schroeder S, Kruger N, Herrler T, Erichsen S, Schiergens TS, Herrler G, Wu NH, Nitsche A, Muller MA, Drosten C, Pohlmann S: SARS-CoV-2 cell entry depends on ACE2 and TMPRSS2 and is blocked by a clinically proven protease inhibitor. Cell 2020, 181:271–280.e8
9. Yinda CK, Port JR, Bushmaker T, Offei Owusu I, Purushotham JN, Avanzato VA, Fischer RJ, Schulz JE, Holbrook MG, Hebner MJ, Rosenke R, Thomas T, Marzi A, Best SM, de Wit E, Shaia C, van Doremalen N, Munster VJ: K18-hACE2 mice develop respiratory disease resembling severe COVID-19. PLoS Pathog 2021, 17:e1009195
10. Oladunni FS, Park JG, Pino PA, Gonzalez O, Akhter A, Allue-Guardia A, et al: Lethality of SARS-CoV-2 infection in K18 human angiotensin-converting enzyme 2 transgenic mice. Nat Commun 2020, 11:6122
11. Seo SM, Son JH, Lee JH, Kim NW, Yoo ES, Kang AR, Jang JY, On DI, Noh HA, Yun JW, Park JW, Choi KS, Lee HY, Shin JS, Seo JY, Nam KT, Lee H, Seong JK, Choi YK: Development of transgenic models susceptible and resistant to SARS-CoV-2 infection in FVB background mice. PLoS One 2022, 17:e0272019
12. Jeong H, Woo Lee Y, Park IH, Noh H, Kim SH, Kim J, et al: Comparison of the pathogenesis of SARS-CoV-2 infection in K18-hACE2 mouse and Syrian golden hamster models. Dis Model Mech 2022, 15:dmm049632
13. Fumagalli V, Rava M, Marotta D, Di Lucia P, Laura C, Sala E, Grillo M, Bono E, Giustini L, Perucchini C, Mainetti M, Sessa A, Garcia-Manteiga JM, Donnici L, Manganaro L, Delbue S, Broccoli V, De Francesco R, D'Adamo P, Kuka M, Guidotti LG, Iannacone M: Administration of aerosolized SARS-CoV-2 to K18-hACE2 mice uncouples respiratory infection from fatal neuroinvasion. Sci Immunol 2022, 7:eabl9929
14. Committee for the Update of the Guide for the Care and Use of Laboratory Animals; National Research Council: Guide for the Care and Use of Laboratory Animals. Eighth Edition. Washington, DC: National Academies Press, 2011

15. Butowt R, von Bartheld CS: The route of SARS-CoV-2 to brain infection: have we been barking up the wrong tree? Mol Neurodegener 2022, 17:20
16. ten Broeke T, Wubbolts R, Stoorvogel W: MHC class II antigen presentation by dendritic cells regulated through endosomal sorting. Cold Spring Harb Perspect Biol 2013, 5:a016873
17. Halfmann PJ, Iida S, Iwatsuki-Horimoto K, Maemura T, Kiso M, Scheaffer SM, et al: SARS-CoV-2 omicron virus causes attenuated disease in mice and hamsters. Nature 2022, 603:687−692
18. Suryawanshi RK, Chen IP, Ma T, Syed AM, Brazer N, Saldhi P, et al: Limited cross-variant immunity from SARS-CoV-2 Omicron without vaccination. Nature 2022, 607:351−355
19. Uhlen M, Fagerberg L, Hallstrom BM, Lindskog C, Oksvold P, Mardinoglu A, et al: Proteomics: tissue-based map of the human proteome. Science 2015, 347:1260419
20. Toulmin SA, Bhadiadra C, Paris AJ, Lin JH, Katzen J, Basil MC, Morrisey EE, Worthen GS, Eisenlohr LC: Type II alveolar cell MHCII improves respiratory viral disease outcomes while exhibiting limited antigen presentation. Nat Commun 2021, 12:3993
21. Steimle V, Siegrist CA, Mottet A, Lisowska-Grospierre B, Mach B: Regulation of MHC class II expression by interferon-gamma mediated by the transactivator gene CIITA. Science 1994, 265:106−109
22. Wijdeven RH, van Luijn MM, Wierenga-Wolf AF, Akkermans JJ, van den Elsen PJ, Hintzen RQ, Neefjes J: Chemical and genetic control of IFNgamma-induced MHCII expression. EMBO Rep 2018, 19:e45553
23. Ahn J, Barber GN: STING signaling and host defense against microbial infection. Exp Mol Med 2019, 51:1−10
24. Liu X, Wei L, Xu F, Zhao F, Huang Y, Fan Z, Mei S, Hu Y, Zhai L, Guo J, Zheng A, Cen S, Liang C, Guo F: SARS-CoV-2 spike protein-induced cell fusion activates the cGAS-STING pathway and the interferon response. Sci Signal 2022, 15:eabg8744
25. Liu W, Reyes HM, Yang JF, Li Y, Stewart KM, Basil MC, Lin SM, Katzen J, Morrisey EE, Weiss SR, You J: Activation of STING signaling pathway effectively blocks human coronavirus infection. J Virol 2021, 95:e00490-21
26. Shen WX, Luo RC, Wang JQ, Chen ZS: Features of cytokine storm identified by distinguishing clinical manifestations in COVID-19. Front Public Health 2021, 9:671788
27. Aghbash PS, Eslami N, Shamekh A, Entezari-Maleki T, Baghi HB: SARS-CoV-2 infection: the role of PD-1/PD-L1 and CTLA-4 axis. Life Sci 2021, 270:119124
28. Galani IE, Andreakos E: Impaired innate antiviral defenses in COVID-19: causes, consequences and therapeutic opportunities. Semin Immunol 2021, 55:101522
29. Saichi M, Ladjemi MZ, Korniotis S, Rousseau C, Ait Hamou Z, Massenet-Regad L, Amblard E, Noel F, Marie Y, Bouteiller D, Medvedovic J, Pene F, Soumelis V: Single-cell RNA sequencing of blood antigen-presenting cells in severe COVID-19 reveals multi-process defects in antiviral immunity. Nat Cell Biol 2021, 23: 538−551
30. Jackson CB, Farzan M, Chen B, Choe H: Mechanisms of SARS-CoV-2 entry into cells. Nat Rev Mol Cell Biol 2022, 23:3−20
31. Beyerstedt S, Casaro EB, Rangel EB: COVID-19: angiotensin-converting enzyme 2 (ACE2) expression and tissue susceptibility to SARS-CoV-2 infection. Eur J Clin Microbiol Infect Dis 2021, 40: 905−919
32. Angeli F, Reboldi G, Verdecchia P: Ageing, ACE2 deficiency and bad outcome in COVID-19. Clin Chem Lab Med 2021, 59: 1607−1609
33. Imai Y, Kuba K, Rao S, Huan Y, Guo F, Guan B, Yang P, Sarao R, Wada T, Leong-Poi H, Crackower MA, Fukamizu A, Hui CC, Hein L, Uhlig S, Slutsky AS, Jiang C, Penninger JM: Angiotensin-converting enzyme 2 protects from severe acute lung failure. Nature 2005, 436: 112−116
34. Kuba K, Imai Y, Rao S, Gao H, Guo F, Guan B, Huan Y, Yang P, Zhang Y, Deng W, Bao L, Zhang B, Liu G, Wang Z, Chappell M, Liu Y, Zheng D, Leibbrandt A, Wada T, Slutsky AS, Liu D, Qin C, Jiang C, Penninger JM: A crucial role of angiotensin converting enzyme 2 (ACE2) in SARS coronavirus-induced lung injury. Nat Med 2005, 11: 875−879
35. Zhao T, Bernstein KE, Fang J, Shen XZ: Angiotensin-converting enzyme affects the presentation of MHC class II antigens. Lab Invest 2017, 97:764−771
36. Verdecchia P, Cavallini C, Spanevello A, Angeli F: The pivotal link between ACE2 deficiency and SARS-CoV-2 infection. Eur J Intern Med 2020, 76:14−20